IEEE Robotics and Automation Letters (RA-L) paper, presented at ICRA 2024, Yokohama, Japan. Cite as RA-L paper.

A Selectively Controllable Triple-helical Micromotor

Hongyu Zhao, Min Ye, Bradley J. Nelson, *Fellow, IEEE,* Xiaopu Wang*, *Member, IEEE*

***Abstract*— Selective control mechanisms of microrobots have attracted significant attention from researchers. So far, selective control within multiple/swarm magnetic microrobots has been achieved with many strategies, such as utilizing locally specified magnetic fields, applying electrostatic anchoring, taking the advantages of geometry/wettability heterogeneity of the microrobots, etc. Using the step-out behavior of helical microrobots driven by a rotating magnetic field, researchers have proposed a mathematical model for multihelical motor that can be selectively controlled. Based on this model, we developed a micromotor that consists of three geometrically heterogeneous helices that can be selectively driven within a specific narrow frequency range. This type of micromotor shows bi-direction motion capability and has the potential to be used as an actuation unit for multiple types of functional micromechanisms.**

I. Introduction

The past two decades have shown rapid development in small-scale robots. From the nanometer to the micrometer scale, a large number of tiny mobile devices have emerged that can achieve diverse motion modalities, such as swimming, crawling, rolling, jumping, sliding, etc. [1-5]. Benefiting from their controllable movabilities and tiny size, these mobile devices have the potential to access confined spaces in the human body, and thus, promise a bright future in precision medicine, particularly for targeted drug/gene delivery and minimally invasive surgery [6-9].

Helical microrobots, inspired by the flagella of bacteria and sperm, are microrobotic prototypes that can be actuated by rotating magnetic fields, and demonstrate excellent mobility in fluids, such as water, blood, etc. [10-12]. Their locomotion mechanism has been widely investigated by researchers. Purcell [13, 14] clarified the basic dynamic model of rotating flagella for the first time. The propulsion matrix he proposed established the linear relationship between angular velocity, the translational velocity of a helix, and the external force as well as torque conducted on it. The locomotion mechanism of helical microrobots has also been further developed and quantified in later research [15-17]. In order to independently control multiple microrobots to achieve more complex tasks, researchers have been focusing on the selective control mechanisms of multiple microrobots [18-21], and in particular, the step-out behavior of helical microrobots. Under a homogenous rotating magnetic field, radial magnetized helical microrobots can follow the rotating magnetic field synchronously when the rotating frequency varies from zero to the step-out frequency. With a further increase in the rotating frequency of the magnetic field, the microrobots can no longer follow the rotation and, correspondingly, the translational velocity of microrobots decays rapidly towards zero. Wang et al. [22] proved that surface chemical characteristics have a significant impact on the step-out frequency and realized independent control of several groups of microrobots in a swarm by controlling their surface wettability. Utilizing the step-out frequency difference of geometric heterogeneous helices, Katsamba and Lauga [23] proposed a freely jointed multihelical motor, theoretically characterized the selective control mechanism of the motor, and constructed an algorithm for designing micromotors with prescribed magnetic response functions. Compared to other works that use a locally specific magnetic field [20] or localized trapping [24], their method provides a more convenient method for creating selectively controllable microrobots. As an example of multihelical micromotors, Giltinan et al. [25] demonstrated a selectively controllable double-helical micromotor and evaluated its motion characteristics. This micromotor has a velocity-frequency profile with two transition points and can be designed to have zero motion until the rotating frequency of the magnetic field reaches its first transition point.

To achieve a more advanced selective micromotor with more transition points in the velocity-frequency profile, we have developed a triple-helical micromotor and experimentally explored its motion performance as well as its frequency selectivity. The triple-helical micromotor consists of three geometrically heterogenous helices and a central rod. The three helices are freely jointed and axially spaced on the central rod. The micromotor can be driven by a uniform rotating magnetic field within a narrow frequency range. With an additional transition point, the propulsion exerted on the entire triple-helical micromotor by rotating magnetic fields when the frequency is below the first transition point or above the third transition point can be ignored. In other words, our triple-helical micromotor can only be driven within its characteristic frequency-response interval. With this feature, these triple-helical micromotors can be used as actuation units for a variety of wireless functional micromechanisms that require selective control, such as microrobotic arms with multi-degree-of-freedom [26], microgrippers [27], microneedles [27], and open-close switchable microboxes for drug release [6].

Micromechanisms with selective controllable actuation units can be simultaneously equipped on a mobile microplatform that can move stably in vasculature in a hemodynamic environment to accomplish multiple tasks, such as the recently reported stent microrobot [6].

Manuscript received: October 26, 2022; Revised: January 7, 2023; Accepted: February 20, 2023. This paper was recommended for publication by Editor Pietro Valdastri upon evaluation of the Associate Editor and Reviewers' comments. This work is supported by Shenzhen Institute of Artificial Intelligence and Robotics for Society (AC01202101106), and the National Natural Science Foundation of China (Grant No. 52305610). (*Corresponding author: Xiaopu Wang*. Asterisk indicates the corresponding author).

Hongyu Zhao, Min Ye, and Xiaopu Wang are all with Shenzhen Institute of Artificial Intelligence and Robotics for Society (AIRS), The Chinese University of Hong Kong, Shenzhen, Guangdong 518129, China. (e-mails: zhaohongyu@cuhk.edu.cn; yemin@cuhk.edu.cn; wangxiaopu@cuhk.edu.cn)

Bradley J. Nelson is with the Institute of Robotics and Intelligent Systems, ETH Zurich, Tannenstrasse 3, Zurich CH-8092, Switzerland. (e-mail: bnelson@ethz.ch)

Digital Object Identifier (DOI): see top of this page.

IEEE Robotics and Automation Letters (RA-L) paper, presented at ICRA 2024, Yokohama, Japan. Cite as RA-L paper.

II. Modeling of Single Helix and Multihelical Motor

A. Single Helix

According to previous research, helical microrobots driven by a rotating magnetic field can travel steadily in fluids. Fig. 1 shows the geometry parameters of a single helix. Parameter θ represents the angle between the local tangential direction and the central axis of the helix, and parameter λ denotes the screw pitch of the helix. Parameters R and r represent the radius of the helix and the radius of the filament of the helix, while parameters n and δ represent the number of turns and the thickness of the magnetic coating film, respectively. The relation between θ and λ is described by $tan\,\theta = 2\pi R\,/\,\lambda$. The total length of the helix is given by $L = 2\pi nR\,/\,sin\,\theta$. The chirality of the helix is symbolized by h, with the value +1 for right-handed and -1 for left-handed helices. The magnetic torque T_m applied on the helix under a magnetic field rotating along the y-axis with a magnetic flux density magnitude B can be summarized as follows:

$$T_{mag} = V\boldsymbol{M} \times \boldsymbol{B} = VMBsin(\omega_r t - \Theta). \tag{1}$$

Here, $V = \pi(r^2-(r-\delta)^2)L$ is the volume of coated magnetic material on the surface of the helix, $\boldsymbol{M}$ is the magnetization, ω_r is the angular velocity of the rotating magnetic field, and Θ is the rotated angle of magnetization direction within time t. The fluid resistance exerted on a helix, swimming at an equilibrium state with velocity v and angular frequency ω, can be derived as:

$$\begin{bmatrix} F_{mag} \\ T_{mag} \end{bmatrix} = \begin{bmatrix} F_{hydr} \\ T_{hydr} \end{bmatrix} = \begin{bmatrix} A & B \\ B & D \end{bmatrix} \begin{bmatrix} v \\ \omega \end{bmatrix}. \tag{2}$$

In this equation, the matrix elements A, B, and D are affected by geometry parameters (R, r, n, θ), surface water contact angle α, tangential resistance coefficients $c_{\parallel}$ and normal resistance coefficient $c_{\perp}$ of the given helix [17]. F_{mag} and T_{mag} are the magnetic force and torque applied on the helix, which are equal to F_{hydr} and T_{hydr} at equilibrium states respectively. When the helix is actuated solely by a rotating magnetic field, the external magnetic force F_{mag} is set to 0, which makes F_{hydr} equal to 0, and T_{hydr} equal to the external magnetic torque T_{mag}. The synchronization behaviour between the helix and the applied magnetic field has been described in literature [17, 28]: when a helix swims steadily in fluids, the angular velocity ω of the helix can be computed as follows:

$$\langle\omega\rangle = \begin{cases} \omega_r & if\ \omega_r < \omega_{SO}, \\ \omega_r\left[1-\sqrt{1-(\omega_{SO}/\omega_r)^2}\right] & if\ \omega_r \geq \omega_{SO}. \end{cases} \tag{3}$$

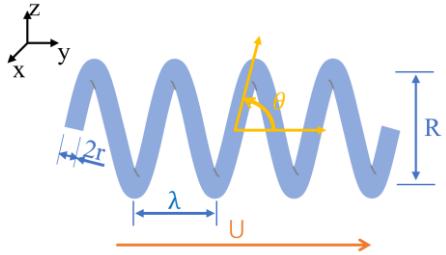

Fig. 1. Illustration of a single helix with the description of its geometric parameters.

Here, $\omega = \frac{d\Theta}{dt}$ is the angular velocity of the helix, ω_r is the angular velocity of the magnetic field, and ω_{SO} is the angular velocity of the helix at the step-out frequency. Translational velocity can be computed as $v = -\frac{B}{A}\omega$. Eq. (3) shows that with the increase of ω_r from zero to ω_{SO}, the helix can rotate synchronously with the field, while ω decreases gradually as ω_r increases above ω_{SO}.

B. Multihelical Micromotor

We designed a multihelical motor based on the fundamental theory of the single helix. By connecting three helices in series without limiting their rotation along their central axis and fixing their relative axial location, a velocity-frequency profile with three transition points can be generated by utilizing the difference in each helix's step-out behavior.

According to Katsamba and Lauga's theory [23], with the helices in the multihelical motor indexed with i (as shown in Fig. 20), Eq. (1-2) can be updated as follows:

$$F_{hydr}^{(i)} = A^{(i)}U + B^{(i)}\frac{d\Theta_i}{dt}, \tag{4}$$

$$T_{hydr}^{(i)} = B^{(i)}U + D^{(i)}\frac{d\Theta_i}{dt}, \tag{5}$$

$$\textstyle\sum_{i=1}^{N} F_{hydr}^{(i)} = 0, \tag{6}$$

$$T_{hydr}^{(i)} = T_{mag}^{(i)} \qquad \forall i, \tag{7}$$

$$T_{mag}^{(i)} = V_i M_i B sin(\omega_r t - \Theta_i). \tag{8}$$

It is notable that the velocity U denotes the velocity of the entire micromotor and also of each helix, as the velocities of every helix along their axes are the same due to the structural restriction. Moreover, compared to the literature [23], the parameters A, B, D used in this work are the updated values that take the influence of surface wettability into account [17], i.e. the calculation of the matrix elements A, B, D covers the coefficient of surface wettability Q ($0.0644\,(180-\alpha)^2$), where α represents the contact angle of the helix. Eq. (4-8) can be transformed into a non-dimensional form, where the quantities in the equations are represented by hat for their nondimensional parts. Combining these equations by eliminating the term $\hat{U}$, they can be transformed into the form of Adler's governing equation [23] (Eq. (9)) to find the approximate equation system for all values of i, while disregarding the relatively small coupling term.

$$\frac{d\,\triangle\,\theta_i}{d\tau} = \hat{\omega} - \hat{\omega}_i sin\,\triangle\,\theta_i \tag{9}$$

Here, $\triangle\,\theta_i = \omega_r t - \theta_i$ is the phase difference between the magnetic field and the magnetization, τ is the nondimensionalized time, and $\hat{\omega}$ is the nondimensional angular velocity of the magnetic field. The symbolization $\hat{\omega}$ is different from that in the literature [23] to avoid confusion of the angular velocity (also called angular frequency) expressed in rad/s and the magnetic rotating frequency expressed in Hz. $\hat{\omega}_i$ represents the angular velocity of the magnetic field at the i-th transition point of the micromotor profile and is given by Eq. (10), where the s_i and c_i are used as the abbreviation of $sin\,\theta_i$ and $cos\,\theta_i$.

IEEE Robotics and Automation Letters (RA-L) paper, presented at ICRA 2024, Yokohama, Japan. Cite as RA-L paper.

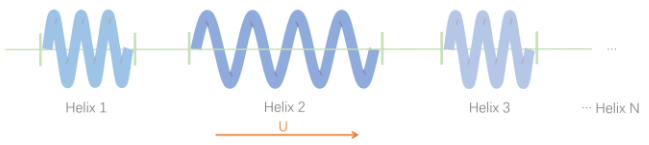

Fig. 2. illustration of a multihelical micromotor. Helices from left to right are notated with index i = 1, 2, 3, … N, respectively.

$$\widehat{\omega}_i = \frac{\widehat{M}_i\left(\left(\hat{r}_i+\hat{\delta}\right)^2-\hat{r}_i^2\right)}{Q\hat{c}_{\perp_i}(\hat{R}_i^2(\rho_i s_i^2+c_i^2)-h_i(1-\rho_i)s_i c_i \hat{R}_i \mathcal{A}_i)} \quad (10)$$

Here, $\mathcal{A}_i$ is the nondimensionalized synthetic characteristic parameter related to all the comprised helices, which can be expressed as

$$\mathcal{A}_i = \frac{2\pi n_i \hat{c}_{\perp_i} h_i(1-\rho_i)cos\theta_i \hat{R}_i^2}{\sum_k 2\pi n_k \hat{R}_k \hat{c}_{\perp_k}(\rho_K cos^2\theta_K + sin^2\theta_k)/sin\theta_k}. \quad (11)$$

Here, ρ denotes the ratio $\hat{c}_{\parallel_i}/\hat{c}_{\perp_i}$, where the $\hat{c}_{\parallel_i}$ and $\hat{c}_{\perp_i}$ are the resistance coefficients in the directions perpendicular and parallel to the local tangent of the centerline of the helices. ρ is approximately set to 0.5 [23], and $\hat{c}_{\perp_i}$ is updated as $\frac{4\pi\hat{\eta}}{ln\left(\frac{0.36\pi\hat{R}_i}{\hat{r}_i sin\theta_i}\right)+0.5}$, where η is the dynamic viscosity of the fluid [17]. $h_i = sign(\mathcal{A}_i)$ is the chirality of i-th helix. $n_i = a/\hat{R}_i$ is the turns of i-th helix, where a is a constant (for the detailed derivation process and description, please refer to the literature [23]).

From the initial time when the external magnetic field overlaps with the magnetization direction of the i-th helix until they overlap again, $\triangle\Theta_i$ changes from 0 to 2π. Assuming the time interval is $\triangle\tau$, the change rate of $\triangle\Theta_i$ depending on time could be expressed as Eq.(12).

$$\frac{d\triangle\Theta_i}{d\tau} \approx \frac{\triangle(\triangle\Theta_i)}{\triangle\tau} = \frac{2\pi}{\int_0^{2\pi}\left(\frac{d\triangle\Theta_i}{d\tau}\right)^{-1} d\triangle\Theta_i}, \quad (12)$$

$$\langle\frac{d\Theta_i}{d\tau}\rangle = \widehat{\omega} - \frac{d\triangle\Theta_i}{d\tau} = \begin{cases} \widehat{\omega} & if\ \widehat{\omega} < \widehat{\omega}_i, \\ \widehat{\omega} - \sqrt{\widehat{\omega}^2 - \widehat{\omega}_i{}^2} & if\ \widehat{\omega} \geq \widehat{\omega}_i. \end{cases} \quad (13)$$

Using Eq. (12), which is in its general form, the average angular velocity of each helix can be obtained as shown in Eq. (13). By substituting Eq. (13) into Eq. (4) and Eq. (6), and then combining these two equations, the velocity U can be acquired as

$$\langle\widehat{U}\rangle = \sum_i \mathcal{A}_i\left[\widehat{\omega} - \mathbf{1}_{\widehat{\omega}>\widehat{\omega}_i}\sqrt{\widehat{\omega}^2 - \widehat{\omega}_i{}^2}\right], \quad (14)$$

where $\mathbf{1}$ represents the indicator function[29], i.e., when the subscript $\widehat{\omega} > \widehat{\omega}_i$, $\mathbf{1}_{\widehat{\omega}>\widehat{\omega}_i}$ is equal to 1, otherwise, this term is equal to 0. By setting the first term $\sum_i \mathcal{A}_i$ to 0, the multihelical micromotor is stationary within an angular velocity interval 0 to $\widehat{\omega}_1$.

For a multihelical micromotor with N helices, there are N transition points, where velocity shows a sudden change. The i-th transition point can be denoted as $(\widehat{\omega}_i, U_i)$ for i from 1 to N. Theoretically, a larger quantity of helices leads to more transition points, so that the velocity-frequency profile of the corresponding multihelical micromotor is more regulatable.

III. Design of Triple-helical Micromotor

Based on the reverse design algorithm introduced in the literature [23], we designed a triple-helical micromotor, which consists of three helices for three transition points, resulting in a sharper peak shape profile compared to that of double-helical micromotors. The parameter $\mathcal{A}_i$ (i from 1 to 3) can be iteratively computed by substituting the angular frequency and the velocity values at three transition points into Eq (14). After getting the parameter $\mathcal{A}_i$ (i from 1 to 3), the chirality h_i can be obtained. Then substituting the calculated values into Eq. (10-11) and predetermining all the values in Eq. (10-11) except the parameters that describe the shape of helices (θ_i and $\hat{R}_i$), by combing six equations, i.e., Eq. (10) and Eq. (11) for i = 1 to 3, the six unknown parameters that determine the shape of helices (θ_i and $\hat{R}_i$ for i = 1 to 3) can be obtained. More specifically, after setting and non-dimensionalizing the velocity values U_i and angular velocity values ω_i of each transition point, the coating thickness δ, the filament radius r_i of each helix, the constant a, the surface water contact angle α, the dynamic viscosity η, the residual magnetization M, and the magnetic strength B, the helical angle θ_i and the radius $\hat{R}_i$ of each helix are calculated with MATLAB by solving the equation system for the reverse design algorithm. Notably, the constant a, which represents the product of n and $\hat{R}_i$ of each helix, is set to the same value for all the helices according to the reduction method of equations in the literature [23] to get a simplified design model. After getting the value of $\hat{R}_i$, the value of n_i can be acquired through $n_i = a/\hat{R}_i$. It is summarized in TABLE I the prescribed parameters, which still should be nondimensionalized before computation. After the solving process, the computed parameter should be dimensionalized and all the computed parameters of the helices are listed in TABLE II. These parameters were finally determined after several design iterations by adjusting the prescribed parameters.

The iterations are necessary to make the equations have solutions and also to ensure suitable helical shapes with sufficient space between the central rod and each helix considering the 3D-printing resolution. Besides, the obtained θ_i and R_i should be in the scale of hundred-micrometers, for easy fabrication and reducing the effect of the viscosity and friction that may result from the scaling law. In each step of the iteration: The coating thickness δ was limited to the maximum value that the evaporation device used in this work can provide. The velocity U_2 of micromotor at the second transition point was set to a relatively high value to get satisfactory mobility. The filament radius r of helices was set to suitable values for sufficient stiffness. The constant a was set to a suitable value to ensure that the helices have a moderate quantity of turns n to guarantee more stable rotation. The frequency values of transition points 1 and 3 were set within the range that the magnetic field generator can provide, and were set to have a narrow range for great frequency selectivity. A brief flowchart for the modeling and design is illustrated in Fig. 3.

TABLE I. Prescribed Parameters of Each Helix/Index

i	r_i (μm)	ω_i (rad/s)	U_i (μm/s)	δ (μm)	α (°)	η (Ns/m²)	a	M (kA/m)	B(mT)
1	51	75	0	1.2	108.2	8.9×10^{-4} (water, at 25°C)	1309	500[25]	15
2	51	105	262.5						
3	41	116.775	0						

TABLE II. COMPUTED GEOMETRIC PARAMETERS OF EACH HELIX

i	R_i (μm)	θ_i (°)	n_i	h_i
1	202.994	83.5064	6.4485	-1
2	159.2126	77.0474	8.2217	1
3	140.1657	83.4929	9.3389	-1

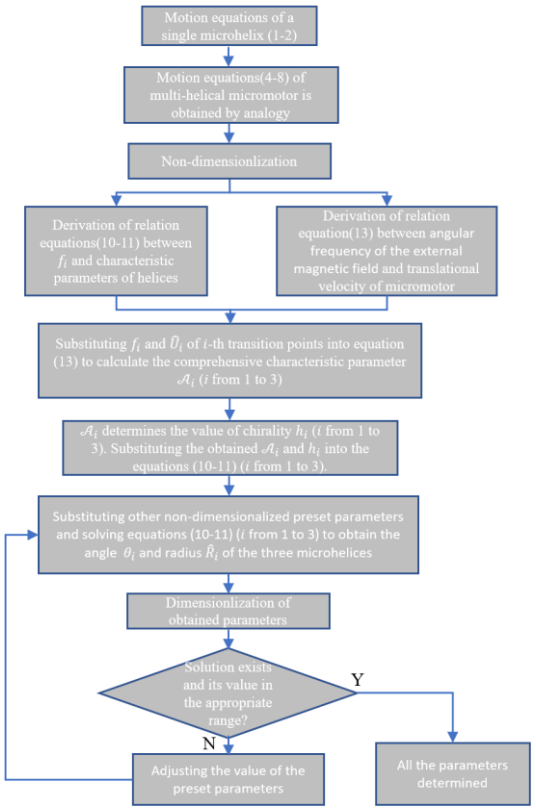

Fig. 3. The flowchart of mathematical modeling and parameter determination process.

Since the coefficients (including ρ, $\hat{c}_\perp$, α, η, etc.) used in the calculation are empirical parameters, there may be a large deviation between the velocity and frequency curve obtained in the calculation and that of the real experiments. Fortunately, these coefficients are natural characteristics, which have a linear or negligible impact on the entire velocity-frequency profile, so they have a negligible influence on the profile trend. Therefore, the profile trend can be illustrated by the normalized velocity-frequency curve. For normalization, the maximum velocity of the micromotor and the frequency of the first transition point are taken as 1. The normalized velocity-frequency profile of the entire triple-helical micromotor is shown in Fig. 4.

In the CAD modeling of the triple-helical micromotor, the three helices were arranged in order using spacing to minimize the interference of their surrounding fluid. Two stop blocks with a ring were incorporated to restrict lateral motion of the entire micromotor. Six disks on the central rod restrict the relative axial motion between the helices. The disks are partially hollowed and connected to the central rod with three ribs with

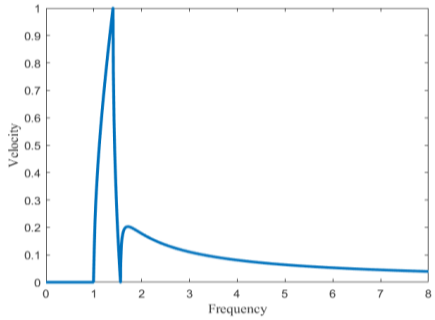

Fig. 4. The velocity-frequency profile of the triple-helical micromotor.

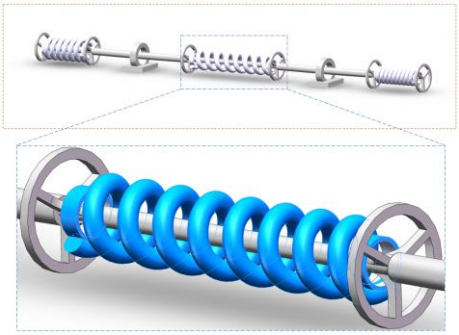

Fig. 5. The CAD model of the triple-helical micromotor. The close-up view of the second helix (highlighted in blue) is to illustrate the details of the helices and central rod.

rounded edges. From the frontal perspective, the disk is shaped like the steering wheel of a car. These disks allow fluid to flow freely to prevent the fluid generated by the helices from influencing the motion of the whole micromotor. The two ends of each helix are equipped with ring structures to stabilize the contact between the helix and disk, thus increasing the stability of the overall motion. The lack of rigidity of the two linkers may influence the performance of the motion behavior by causing more vibration and instability of the contact between the micromotor and substrate. It will also cause the long axes of helices cannot to align with each other. So sufficient rigidity must be guaranteed through suitable structural design (e.g. the thickness and size) to ensure the pure axial motion of the entire micromotor. The final design of the triple-helical micromotor is illustrated in Fig. 5.

IV. FABRICATION

The triple-helical micromotor was fabricated on silicon slice substrates with a commercial photoresist IP-Dip by two-photon lithography technology using the Nanoscribe Photonic Professional GT2 device (Nanoscribe GmbH). This 3D-printing device has a high resolution of 200 nm (using a 63 × objective) for small and delicate features and also can create features at a millimeter scale rapidly using a 25 × or a 10 × objective with a faster speed but lower resolution. IP-Dip is a liquid negative resin formulation provided by Nanoscribe GmbH, which has a great printing effect for the finest features. Its elastic modulus is 2.91 Gpa and its viscosity is 2,420 MPa (at 20°C).

A. Overhanging and Flying Features

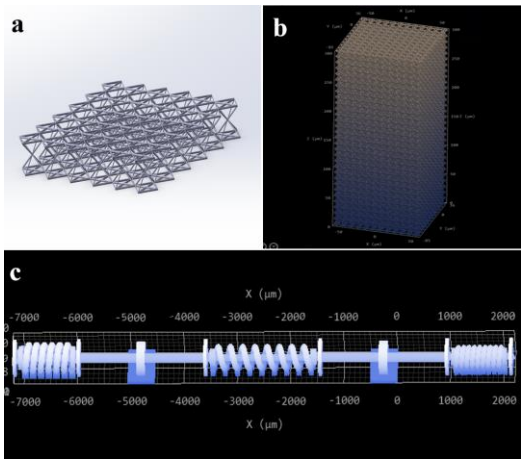

Fig. 6. (a) A single layer of the lattice support structure; (b) The multi-layer lattice support pillar used in the fabrication; (c) The micromotor supported by lattice pillars with distinct geometric parameters that adapt to the contours of their supporting structures.

As shown in Fig. 5, the micromotor comprises freestanding features (three helices), overhanging features (the backbone and tendon), and a large-span feature (the central rod), and had to be split into multiple blocks due to the size limit of the printing field, leading to complexities in the printing process. We tested several approaches for printing the overhanging and fly features and finally selected the method proposed by Gross et al. [30] of utilizing lattice support structures. As shown in Fig. 6, lattice support structures were designed and printed to hold the three helices. The geometric parameters of each supporting pillar were set based on the contours of the entire micromotor and verified over repeated printing cycles. The issue of the overhanging features also had to be resolved for the long-span central rod of the micromotor. In the standard printing process, structures are stacked in layers. This can result in sagging in the printing process, particularly for a large-span structure with overhanging features. In addition, the standard printing process can affect the printing quality of the central rod (printed in spilled blocks) and cause adhesion between the helices and the rod, as experienced in the printing test. Therefore, the central rod was printed independently and its printing direction was adjusted from an upright stack to a horizontal stack using fine block splitting to overcome the issue of the overhanging features. Since the printing quality would be reduced because of shifts in the focus point position and laser energy attenuation that occur when the laser passes through the printed structure, the printing sequence of the micromotor was determined as: the lower half of the helices first, then the central rod, and finally the upper half of the helices.

B. Printing Parameters and Postprocessing

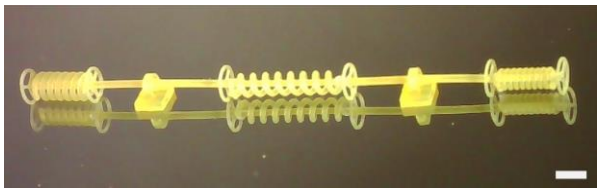

Fig. 7. A photo of the fabricated triple-helical micromotor. The scale bar is 500 μm.

To ensure high printing accuracy and lower time costs, the lattice support structures were first printed with 63 × objective, and then the entire micromotor was printed with 10 × objective. Alignment through two markers was conducted after changing the objectives. The printing speed and laser power were set as 20,000 μm/s and 50 mW, respectively. The printing process requires about 15 h in total (10 h for the lattice support structures and 5 h for the micromotor). After printing, the obtained sample was developed in Propylene glycol monomethyl ether acetate (PGMEA) for 7 min and then in Isopropyl alcohol (IPA) for 5 min. The short developing time facilitates low structure swelling. The sample was then dried using nitrogen. Finally, the sample was etched in an air plasma atmosphere for 60 min with a flow rate of 200 ml/min and a power of 170 W to remove the support structures. The resulting structure is shown in Fig. 7. Using a probe, we verified that the helices can rotate freely around the central rod and the entire micromotor can move freely from left to right within the constraint region of the two stop blocks.

C. Magnetic Film Coating and Hydrophobic Treatment

Physical vapor deposition (PVD) was employed using a resistive evaporator to deposit magnetic cobalt on the helices, and the deposition thickness was set as 1.2 μm. Titanium (10 nm) was then deposited on top of the cobalt layer to ensure fluorosilane modification in the next step. During the deposition, the holding plate was set to rotate at 20 rad/s, and the rotating plate was set to a tilt angle of 30° to ensure an even distribution of the deposited materials on the helices. After the deposition, the sample was left to rest in air for 4 h, and a TiO_2 layer with several nanometer thicknesses formed naturally on the Titanium layer. For the fluorosilane modification [32], 4.9 ml of ethylene glycol was added to 5ml of deionized water, and 0.1ml of 1H,1H,2H,2H-perfluorodecyltrimethoxysilane was then added slowly. The mixture was then magnetically stirred to a uniform state. Dilute hydrochloric acid was added to maintain a pH value of approximately 3.0. After stirring for 1h, the fluorosilane was evenly dispersed, and the fluorosilane was then fully hydrolyzed by allowing it to stand for 5 h. The 3D-printed sample was then placed in the hydrolyzed fluorosilane solution to make the fluorosilane graft on the surface of the TiO_2 layer on the sample. Fluorosilane modification of the surface helps to reduce surface energy, so that friction, adhesion, and fluidic drag are reduced during the motion of the microhelices.

The surface water contact angle (α) of the micromotor was measured as 108.2°by testing a flat segment, which had undergone the same treatments as the sample (including resin coating, magnetic film depositions, and hydrophobic treatment). This result confirms the successful coating of the hydrophobic fluorosilane layer on the sample surface. The tested value of α was considered in the calculation for the geometric design of the micromotor. The increase in α facilitates the reduction of friction and fluid drag, and therefore improves the motion

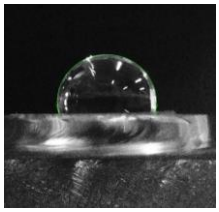

Fig. 8. Measurement of α after fluorosilane treatment. The measurement was conducted using a freely available plug-in in ImageJ-LBADSA [31].

performance of the micromotor. Fig. 8 shows the measurement process of α.

V. Motion Testing

The micromotor was firstly radially magnetized under a 1.8 T magnetic field and the residual magnetization of the micromotor was determined as ~500 kA/m according to the literature [25]. After that, the micromotor was placed on a glass substrate, on which the bottoms of the stop blocks were attached. Then, the substrate was attached to the bottom of a petri dish, which is filled with deionized water afterward. The motion of the micromotor was tested under a rotating magnetic field (15 mT) provide by a MFG-100-I magnetic field generator (Magnebotix AG, Swiss). A series of frequencies from 0 Hz to 100 Hz was used during the testing, and the sampling density was selected to increase with the increasing variation rate of the translational velocity. Multiple tests were executed for each frequency, and the result is represented by the average value and standard variance. Both the clockwise rotating magnetic field and the counterclockwise rotating magnetic field were used to prove the forward and reverse movability of the micromotor. As shown in Fig. 9 the velocity-frequency curves verified the frequency selectivity of the micromotor in both clockwise and counterclockwise cases. The percentage bars indicate that the difference between the counterclockwise (CCW) case and the clockwise (CW) case is small when the velocity values are both high. In contrast, the difference would be prominent when the velocity values are both low, as the measurement error and the error caused by friction dominate in this case.

Theoretically, the forward and reverse motion characteristics should be the same, due to the symmetric motion profile of each helix when the direction of the magnetic field rotation is inverted. However, it is almost impossible to fabricate a perfect symmetric triple-helical micromotor due to the complex design of the micromotor and the current fabrication technology. Therefore, a difference exists between the CCW case and the CW case, as shown in Fig. 9.

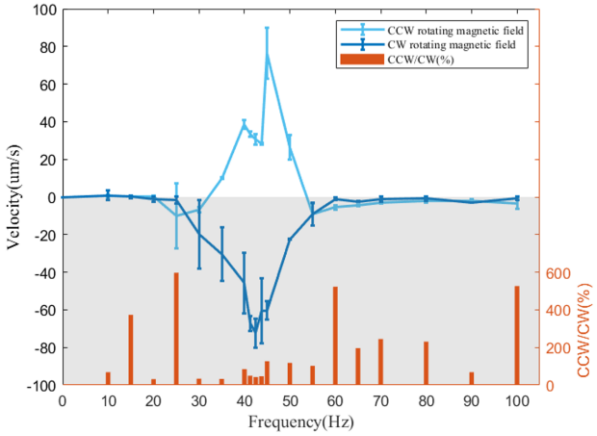

Fig. 9. The velocity-frequency profile of the triple-helical micromotor. The cyan curve denotes the CCW case, and the blue curve denotes the CW case. The orange bars at the bottom reflect the absolute value of the velocity ratio of the CCW case and CW case in percentage. The y-axis on the left side stands for the scale mark for the velocity of the micromotor, and the y-axis on the right side stands for the scale mark for the percentage ratio of bars.

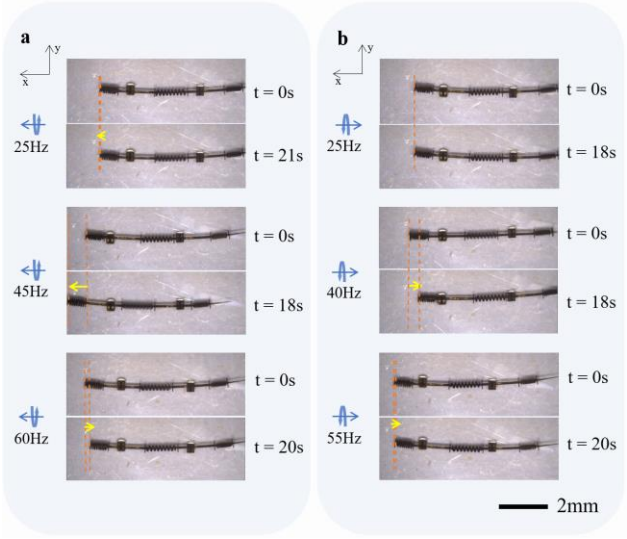

Fig. 10. (a) The motion of the triple-helical micromotor at 25Hz, 45Hz, and 60 Hz, under a counterclockwise rotating magnetic field of 15 mT. (b) The motion of the triple-helical micromotor at 25 Hz, 40 Hz, and 55 Hz, under a clockwise rotating magnetic field of 15 mT. The scale bar is 2mm. Note: the slight bending of the central rod was caused by the swelling of the polymerized IP-Dip resin when it experienced a high temperature during the etching process. The corresponding video is in the supporting information.

When applying a counterclockwise rotating magnetic field, where the rotating frequency was lower than 30 Hz, the micromotor rarely showed movement. When the frequency of the rotating magnetic field was increased to more than 35 Hz, there was a significant increase in the moving speed. At the frequency of 45 Hz, the micromotor had a maximal motion speed of ~76 μm/s. When the frequency was increased over 55 Hz, the velocity decayed rapidly to around 0. Fig. 10(a) shows the corresponding motion at 25 Hz, 45 Hz, and 60 Hz. The reverse movability was also evaluated under a clockwise rotating magnetic field. The micromotor shows the capability of reverse motion similar to its forward motion, as described above. Within the interval 0-30 Hz, the velocity of the micromotor is negligible. Within the interval 25-55 Hz, the velocity has a peak-shape profile with a maximal motion speed of ~72 μm/s. When the frequency is greater than 55 Hz, despite the rebound of the curve, the velocities are relatively small and can be considered negligible when compared to the peak value. Fig. 10(b) shows the corresponding motion at 25 Hz, 40 Hz, and 55 Hz.

Compared with the design theory, the velocity-frequency profile has the same trend as that of the actual experiment. However, the real data has less maximal motion speed and higher boundary frequencies. In addition to the deviation formed during the calculation explained previously, there was also a deviation caused in the actual experiment. This could be due to an insufficient magnetization process, the existence of friction between the helices and the central rod, the wall effect, the fluid interference among all the helices, and/or the peeling of magnetic layers that could occur during the hydrophobic treatment. Likewise, slight bending of the central rod caused by a fabrication error could also lead to a deviation. Despite these deviations, the overall trend is in line with expectations.

Within a certain rotating magnetic field, the triple-helical micromotor designed in this work can be only driven within a specific narrow frequency range. Benefiting from this property,

when multiple triple helical micromotors with different designs are placed within the same workspace, we can selectively turn on one of them, while keeping the other ones off. In another word, selective control within a group of triple helical micromotors can be realized. Besides, the micromotor's forward and backward motions have similar profiles, and their narrow response frequency ranges resemble, although the existence of some anisotropic frictions between the helix and the central rod. These two properties mentioned above enable a triple-helical micromotor to be actuated independently for executing reversible tasks, while other triple-helical micromotors in the same workspace are not activated. For instance, a specific micromotor can be selected from a group of them to control the open and close state of a drug-loaded box, the tension and relaxation of robotic joints, or other mechanisms with bi-state or multi-state.

VI. Application Demonstration

The triple-helical micromotor can be used as an actuation unit for micromechanisms. In this work, it is demonstrated that a triple-helical micromotor as shown in Fig. 11(a) can be used to pull a tendon-driven continuum microactuator selectively within a certain frequency range. The micro-actuator connected with the triple-helical micromotor through an extended actuation tendon was fabricated by two-photon polymerization. Fig. 11(b) shows the close-up view of the fabricated micro-actuator. Here are some parameters of the micro-actuator part, disk radius $R_{enddisk}$ = 220 μm, backbone length L = 1600 μm, elastic modulus E = 2.91 Gpa, and area moment of inertia I = 4.97e-21 m^4. The illustration of the entire micromechanism is shown in Fig. 11a. During the magnetic film coating step, the actuator part was covered to selectively coat only the micromotor. For a better pulling effect, the thickness of the magnetic coating film was set to the maximum value of the evaporator (1.6μm), which is 1.33 times higher than the value in TABLE I. To prevent the magnetic layer from peeling off, the hydrophobic treatment was canceled. As a result of these changes, the velocity-frequency profile of the micromotor used here shrinks proportionally, compared to the profile shown in Fig. 9. Within a 15 mT rotating magnetic field, the response frequency range of the micromotor is 15 Hz-25 Hz, and a maximum deflection angle θ = 8° of the tendon-driven continuum micro-actuator can be achieved at 20 Hz, as shown in Fig. 11(c). The pulling force (F_{pull}) exerted on the micro-actuator can be calculated based on the Euler-Bernoulli beam equation,

$$\theta = \frac{F_{pull} R_{enddisk} L}{EI}. \quad (15)$$

The calculation result shows that F_{pull} approximately equals 5.737 μN. Because of the existing friction between the tendon and the disk of the actuator, the force supplied by the micromotor should be the sum of friction and F_{pull}.

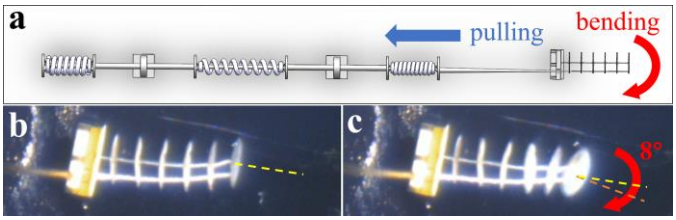

Fig. 11. (a) Illustration of a micromechanism that consists of a tendon-driven continuum micro-actuator and a triple-helical micromotor. (b) The initial state of the micro-actuator part. The slight bending of the backbone at the initial state is caused by the fabrication error. (c) Bending performance of the micro-actuator part within a rotating magnetic field (15 mT, 20 Hz). The deflection (8°) is illustrated with a red arrow, where the yellow and orange dash lines stand for the vertical direction of the end disk at the initial state and the pulled state, respectively.

VII. Conclusion

In this work, we developed a triple helical micromotor based on Katsamba and Lauga's theory and tested its motion performance to verify its frequency-selective characteristics. The support structure and printing sequence are essential for printing the overhanging and freestanding structures. The etching process provides a method for removing the supporting structure without manual operation, thus avoiding possible defects in the microstructure. Experiments suggest that the triple helical micromotor could supply an expected sharp ascent and descent velocity-frequency profile within a determined frequency interval, which would benefit the future expansion of the quantities of the selectively controllable units. The sharp velocity-frequency profile and narrow range of driving frequencies mean that similar selective controllable driving units could be controlled within the limited frequency range of a magnetic field-generating device. The triple-helical motor developed in this work shows bi-direction motion capability, holding the possibility to selectively and linearly drive other micromechanisms.

References

[1] L. Zhang, J. J. Abbott, L. Dong, B. E. Kratochvil, D. Bell, and B. J. Nelson, "Artificial bacterial flagella: Fabrication and magnetic control," Applied Physics Letters, vol. 94, no. 6, 2009.

[2] W. Hu, G. Z. Lum, M. Mastrangeli, and M. Sitti, "Small-scale soft-bodied robot with multimodal locomotion," Nature, vol. 554, no. 7690, pp. 81-85, 2018.

[3] C. Li et al., "Fast and programmable locomotion of hydrogel-metal hybrids under light and magnetic fields," Science Robotics, vol. 5, no. 49, p. eabb9822, 2020.

[4] Y. Alapan, U. Bozuyuk, P. Erkoc, A. C. Karacakol, and M. Sitti, "Multifunctional surface microrollers for targeted cargo delivery in physiological blood flow," Science Robotics, vol. 5, no. 42, p. eaba5726, 2020.

[5] A. Aghakhani, O. Yasa, P. Wrede, and M. Sitti, "Acoustically powered surface-slipping mobile microrobots," Proceedings of the National Academy of Sciences, vol. 117, no. 7, pp. 3469-3477, 2020.

[6] T. Wang et al., "Adaptive wireless millirobotic locomotion into distal vasculature," Nature communications, vol. 13, no. 1, pp. 1-17, 2022.

[7] X. Wang et al., "MOFBOTS: metal‐organic‐framework‐based biomedical microrobots," Advanced Materials, vol. 31, no. 27, p. 1901592, 2019.
[8] F. Qiu, S. Fujita, R. Mhanna, L. Zhang, B. R. Simona, and B. J. Nelson, "Magnetic helical microswimmers functionalized with lipoplexes for targeted gene delivery," Advanced Functional Materials, vol. 25, no. 11, pp. 1666-1671, 2015.
[9] G. Chatzipirpiridis et al., "Electroforming of implantable tubular magnetic microrobots for wireless ophthalmologic applications," Advanced healthcare materials, vol. 4, no. 2, pp. 209-214, 2015.
[10] V. Magdanz, M. Medina‐Sánchez, L. Schwarz, H. Xu, J. Elgeti, and O. G. Schmidt, "Spermatozoa as functional components of robotic microswimmers," Advanced Materials, vol. 29, no. 24, p. 1606301, 2017.
[11] X. Wang et al., "3D printed enzymatically biodegradable soft helical microswimmers," Advanced Functional Materials, vol. 28, no. 45, p. 1804107, 2018.
[12] Q. Wang, X. Du, D. Jin, and L. Zhang, "Real-Time Ultrasound Doppler Tracking and Autonomous Navigation of a Miniature Helical Robot for Accelerating Thrombolysis in Dynamic Blood Flow," ACS nano, vol. 16, no. 1, pp. 604-616, 2022.
[13] E. M. Purcell, "Life at low Reynolds number," American journal of physics, vol. 45, no. 1, pp. 3-11, 1977.
[14] E. M. Purcell, "The efficiency of propulsion by a rotating flagellum," Proceedings of the National Academy of Sciences, vol. 94, no. 21, pp. 11307-11311, 1997.
[15] J. J. Abbott et al., "How should microrobots swim? " The international journal of Robotics Research, vol. 28, no. 11-12, pp. 1434-1447, 2009.
[16] K. E. Peyer, S. Tottori, F. Qiu, L. Zhang, and B. J. Nelson, "Magnetic helical micromachines, Chemistry–A European Journal, vol. 19, no. 1, pp. 28-38, 2013.
[17] X. Wang, C. Hu, S. Pané, and B. Nelson, "Dynamic modeling of magnetic helical microrobots," IEEE Robotics and Automation Letters, vol. 7, no. 2, pp. 1682-1688, 2021.
[18] E. Diller, J. Giltinan, and M. Sitti, "Independent control of multiple magnetic microrobots in three dimensions," The International Journal of Robotics Research, vol. 32, no. 5, pp. 614-631, 2013.
[19] S. Chowdhury, W. Jing, and D. Cappelleri, "Towards independent control of multiple magnetic mobile microrobots," Micromachines, vol. 7, no. 1, p. 3, 2015.
[20] J. Rahmer, C. Stehning, and B. Gleich, "Spatially selective remote magnetic actuation of identical helical micromachines," Science Robotics, vol. 2, no. 3, p. eaal2845, 2017.
[21] T. Xu, C. Huang, Z. Lai, and X. Wu, "Independent control strategy of multiple magnetic flexible millirobots for position control and path following," IEEE Transactions on Robotics, 2022.
[22] X. Wang et al., "Surface-chemistry-mediated control of individual magnetic helical microswimmers in a swarm," ACS nano, vol. 12, no. 6, pp. 6210-6217, 2018.
[23] P. Katsamba and E. Lauga, "Micro-tug-of-war: A selective control mechanism for magnetic swimmers," Physical Review Applied, vol. 5, no. 6, p. 064019, 2016.
[24] C. Pawashe, S. Floyd, and M. Sitti, "Multiple magnetic microrobot control using electrostatic anchoring," Applied Physics Letters, vol. 94, no. 16, p. 164108, 2009.
[25] J. Giltinan, P. Katsamba, W. Wang, E. Lauga, and M. Sitti, "Selectively controlled magnetic microrobots with opposing helices," Applied Physics Letters, vol. 116, no. 13, p. 134101, 2020.
[26] T. Zhang, L. Yang, X. Yang, R. Tan, H. Lu, and Y. Shen, "Millimeter‐Scale Soft Continuum Robots for Large‐Angle and High‐Precision Manipulation by Hybrid Actuation," Advanced Intelligent Systems, vol. 3, no. 2, p. 2000189, 2021.
[27] C. Hong et al., "Magnetically actuated gearbox for the wireless control of millimeter-scale robots," Science Robotics, vol. 7, no. 69, p. eabo4401, 2022.
[28] A. W. Mahoney, N. D. Nelson, K. E. Peyer, B. J. Nelson, and J. J. Abbott, "Behavior of rotating magnetic microrobots above the step-out frequency with application to control of multi-microrobot systems," Applied Physics Letters, vol. 104, no. 14, p. 144101, 2014.
[29] B. B. Mandelbrot, "Co-indicator functions and related $1/f$ noises," in Multifractals and $1/f$ Noise: Springer, 1999, pp. 215-246.
[30] A. J. Gross and K. Bertoldi, "Additive manufacturing of nanostructures that are delicate, complex, and smaller than ever," Small, vol. 15, no. 33, p. 1902370, 2019.
[31] A. F. Stalder, T. Melchior, M. Müller, D. Sage, T. Blu, and M. Unser, "Low-bond axisymmetric drop shape analysis for surface tension and contact angle measurements of sessile drops," Colloids Surfaces A: Physicochemical Engineering Aspects, vol. 364, no. 1-3, pp. 72-81, 2010.
[32] D. P. Long, J. R. Xue, and Z. X. Yan, "Fabrication and characterization of Superhydrophobic film on Titanium substrate," in Advanced Materials Research, 2014, vol. 834, pp. 29-32: Trans Tech Publ.